

The HELLAS2XMM survey: VI. X-ray absorption in the 1df AGN sample through a spectral analysis. [★]

G.C. Perola^{1,2}, S. Puccetti^{1,3}, F. Fiore¹, N. Sacchi², M. Brusa^{4,5}, F. Cocchia^{1,3}, A. Baldi⁶, N. Carangelo⁷, P. Ciliegi⁵, A. Comastri⁵, F. La Franca², R. Maiolino⁸, G. Matt², M. Mignoli⁵, S. Molendi⁶, C. Vignali⁵

¹ INAF, Osservatorio Astronomico di Roma, via Frascati 33, Monteporzio-Catone (RM), 00040 Italy

² Dip. di Fisica, Università Roma Tre

³ Dip. di Fisica Università di Roma Tor Vergata

⁴ Dip. di Astronomia Università di Bologna

⁵ INAF-Osservatorio Astronomico di Bologna

⁶ Harvard-Smithsonian Center for Astrophysics

⁷ IASF/CNR Milano

⁸ INAF-Osservatorio Astrofisico di Arcetri

January 22, 2004

Abstract. The spectroscopic analysis of 117 serendipitous sources in the HELLAS2XMM 1df (1 degree field) survey is described. Of these, 106 sources, of which 86% have a spectroscopic redshift, are used to evaluate the fraction of X-ray absorbed ($\log N_H > 22$) Active Galactic Nuclei (AGN) in the 2–10 keV flux range $0.8\text{--}20 \times 10^{-14}$ erg cm⁻² s⁻¹. This fraction turns out lower than what is predicted by two well known Cosmic X-Ray Background synthesis models, and the discrepancy is significant at the 99.999% level. This result consolidates the findings recently obtained by other authors. In the flux interval explored, the data are consistent with an intrinsic distribution of the absorbing columns (flat per decade above $\log N_H > 21$) independent of luminosity and redshift, together with an AGN luminosity function evolving purely in luminosity. It is shown that, on the other hand, extrapolation to lower fluxes fails to reproduce the results inferred from the Chandra Deep Field North survey. It is found that about 40% of the high luminosity sources in our sample have best fit $\log N_H > 22$, and the surface density of these X-ray obscured QSOs can then be estimated at about 48 per square degree, at the flux limit of $\sim 10^{-14}$ erg cm⁻² s⁻¹ of the HELLAS2XMM 1df survey. As a side issue, 5 or 6 out of 60 sources, that is about 10%, identified with broad line AGN, turn out to be affected by $\log N_H > 22$ absorption.

Key words. X-ray: background, X-ray: surveys, X-ray: AGN

1. Introduction

After the success of ROSAT (Hasinger et al. 1998) in resolving about 75% of the X-ray background (XRB) in the 0.5–2 keV band into sources largely associated with Active Galactic Nuclei (AGN), the satellites Chandra and XMM-Newton achieved a similar result, up to at least 85% of the XRB, in the 2–10 keV band (Mushotzky et al. 2000, Giacconi et al. 2001, 2002, Hasinger et al. 2001; Alexander et al. 2003; see also Moretti et al. 2003 and references therein). The combination of the results in the two bands provides also the observational support for the intuition by Setti & Woltjer (1989) that the XRB could be explained by a dominant contribution of AGN, affected by photoelectric obscuration in different proportions over a wide range of gas columns N_H . This suggestion led to several attempts, all formally successful, to synthesize the

XRB starting from somewhat different assumptions about the AGN Luminosity Function (LF) and its cosmological evolution, and N_H distributions (e.g. Comastri et al. 1995, Gilli et al. 2001, Wilman & Fabian 1999, Miyaji et al. 2000, Ueda et al. 2003). In this context, an important issue, which is being explored with increasingly more detailed X-ray spectral analysis and spectroscopic identification of the optical counterparts, is the fraction of sources with different intrinsic N_H as a function of their flux. This approach provides very strong constraints, especially when accompanied by the study of the LF performed using the same data (e.g. Ueda et al. 2003). The present limits are set by progressively poorer statistics in the X-ray spectra and in the optical spectroscopic identification as one goes to fainter sources. Thus, while a treatment as just outlined, based on the full ensemble of sources utilized by Fiore et al. (2003, hereafter Paper IV), is deferred to La Franca et al. (in prep.), this paper aims to exclu-

sively present the information on the fraction of sources affected by different levels of X-ray obscuration, down to a limit in F(2-10 keV) of about 10^{-14} erg cm $^{-2}$ s $^{-1}$ (corresponding to about 35% of the XRB), extracted from the HELLAS2XMM 1df sample. This sample comprises 117 sources, 93 of them (80%) with a spectroscopic redshift available.

The spectral counts extraction is described in Sect. 2, their best fit analysis in Sect. 3, the synthesis of the results in Sect. 4. Sect. 5 is devoted to a discussion of the results compared to XRB synthesis models, Sect. 6 to the conclusions.

2. Extraction of the spectral counts

The HELLAS2XMM 1df (1 degree field) sample is composed of 122 sources (Paper IV), serendipitously detected in the 2-10 keV band in five XMM-Newton fields: PKS 0537-286, PKS 0312-770, A2690, G158-100, Mrk 509 (see Baldi et al. 2002, for the epochs and exposure times). The observations were performed with the European Photon Imaging Camera (EPIC), composed by one pn back-illuminated CCD array (Strüder et al. 2001) and by two mos front-illuminated CCD arrays (Turner et al. 2001), named mos1 and mos2 respectively. However only the fields PKS 0537-286, PKS 0312-770, A2690 have been observed with the three cameras, whereas the G158-100, Mrk 509 fields have been observed with mos1 and mos2 alone.

The source counts in each camera have been obtained using the events files, in the energy range 0.5-10 keV for the pn and 0.3-10 keV for the mos. The counts of the two mos cameras were eventually combined. The counts of each source have been extracted in a circular region with a radius in the range 20''–40''. In general the radius value was chosen so that the S/N ratio was roughly optimized, but in a few cases this choice was limited by the presence of nearby sources, or by a peculiar position of the source on the detector, for example close to a gap in the CCD array. In some cases the source was detected, and the corresponding counts extracted, only in either the pn or in one or both of the mos cameras, because pn and mos do not cover exactly the same sky regions, and the position of the gaps differs in the pn, mos1 and mos2 CCD arrays.

The background counts for each source were extracted from the nearest source-free region. In doing so, areas near gaps in the CCD array and near the edge of the telescope field of view have been excluded, as well as regions containing hot pixels and other CCD cosmetic defects.

The ancillary response files were generated for each source by means of the tool ARFGEN (SAS 5.4.1¹), in order to properly correct for energy dependent vignetting and point spread function. The response matrix file, updated

for all the observation modes to January 29, 2003 and available at the XMM-Newton archive², was adopted.

Among the 122 sources in Paper IV, the one identified with a star (05370006) was discarded from the start. For the two extended sources, 03120008 and 26900013, the spectral analysis revealed the presence of an AGN contribution in the first, which was therefore kept in the sample. Moreover, only pn and mos spectra with combined counts greater than 40 were considered, and the sources 05370159, 05370164 and 03120116 were therefore discarded.

In summary, the sample studied in this paper is composed of 117 sources, with a spectroscopic redshift available for 93 of them, as reported in Paper IV.

3. Spectral fits

The spectral counts, when higher than about 120, were first accumulated in energy bins with 20 counts each, from 0.3 keV to 10 keV in the mos, and from 0.5 to 10 keV in the pn. They were then fitted, using XSPEC (version 11.2.0) and the χ^2 statistic, with the simple model comprising, in addition to the known galactic absorption: (1) a power law, with two parameters, normalization and photon spectral index Γ ; (2) the absorption N_H at the redshift of the optical counterpart; when both pn and mos data were available, their relative normalization mos/pn was left free to vary between 0.8 and 1.2. This interval was chosen conservatively wider than applicable on-axis, because for sources off-axis a fully reliable intercalibration is still lacking. When the spectral counts were lower than about 120, the C statistic (Cash 1979) was used instead, as implemented in XSPEC (Arnaud 2003³) after background subtraction (see Alexander et al. 2003a for a similar procedure) and with 5 counts in each energy bin (the latter choice was made only for convenience; it does not impair the correct use of the embedded statistics when using the abovementioned XSPEC implementation). In this case the normalization mos/pn was set equal to 1.

The systematic use of the simple model is meant to yield an 'effective' value for the absorbing column, the best one can obtain with the relatively modest statistics available. In addition, it should be stressed that this is after all the most meaningful quantity for the implications that absorption has on the synthesis of the X-ray background.

The galactic absorption columns adopted (see Baldi et al. 2002) are: 8×10^{20} cm $^{-2}$ for the field PKS0312, 2×10^{20} cm $^{-2}$ for A 2690, 2.1×10^{20} cm $^{-2}$ for PKS0537, 4×10^{20} cm $^{-2}$ for Mkn 509, 2.5×10^{20} cm $^{-2}$ for G158–100.

The sources with a spectroscopic redshift and those without were treated separately, and the whole set was subdivided into five subsets. The first subset (S1) com-

¹ http://xmm.vilspa.esa.es/external/xmm_sw_cal/sas_frame.shtml

² <ftp://xmm.vilspa.esa.es/pub/ccf/constituents/extras/responses/>

³ K.A. Arnaud, 2003, "XSPEC User Guide for version 11.3" <http://heasarc.gsfc.nasa.gov/docs/software/lheasoft/xanadu/xspec/manual/manual.html>

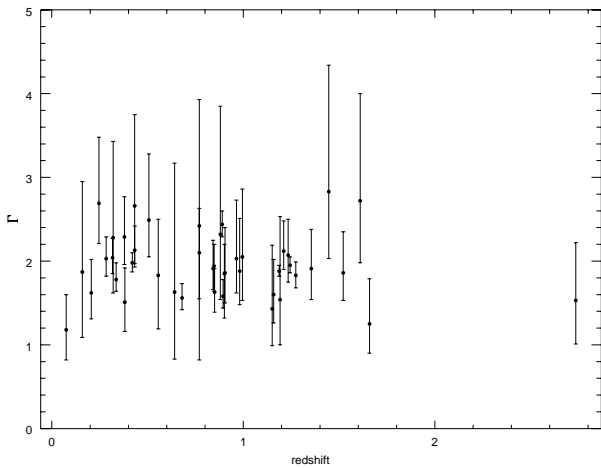


Fig. 1. The spectral index Γ of the S1 sources as a function of redshift.

prises spectra of objects with known z , whose number of degrees of freedom (dof) is equal to or larger than 8 when both Γ and N_H are left as free parameters, and the mos/pn normalization is frozen to its best fit value before estimating the errors. This corresponds to a total number of counts equal to or larger than 220. The 90% confidence intervals on N_H and Γ were therefore calculated with $\Delta\chi^2 = 4.61$. The results for the 44 S1 sources are presented in Table 1, where the following information is given: in Col. 2 the optical classification (AGN1 and AGN2 with their usual meaning, but see Paper IV, ELG = Emission Line Galaxy, ETG = Early Type Galaxy; the few objects reclassified differently from Paper IV are starred), in Col. 3 the redshift, in Col. 4 the instrument(s) used (pm = pn and mos combined), in Col.s 5, 6 and 7, N_H , Γ and χ^2/dof , in Col. 8 the 2-10 keV flux F as observed (when applicable, the mean of the pn and mos values), in Col. 9 the same corrected for the absorption F_u , and the corresponding luminosity in Col. 10, computed using a cosmology with $H_0 = 70 \text{ km s}^{-1} \text{ Mpc}^{-1}$, $\Omega_m = 0.3$ and $\Lambda = 0.7$, and the K-correction appropriate for the best fit value of Γ . Note that throughout the next sections F_u will be used.

The distribution of Γ from Table 1 is given in Fig. 1 as a function of the redshift. The linear correlation coefficient between the two quantities is -0.094, thus any significant dependence on the redshift can be excluded. The sample was then used to evaluate the weighted mean of the spectral index, which is equal to 1.90, with a dispersion equal to ± 0.22 . This justifies the adoption, which follows, of the fixed value $\Gamma=1.9$ for sources with poorer photon statistics.

The second subset (S2) comprises objects with known z but fewer counts, hence with spectral fits now performed with Γ held fixed at 1.9. It includes spectra that, with the best fit normalization mos/pn frozen before error computing, have $4 \leq \text{dof} \leq 8$. For these spectra the 90% confidence interval on N_H was computed with $\Delta\chi^2 = 2.7$. The results for the 36 S2 sources are presented in Table

2, with the same structure as Table 1. We note that the source 03120008, with 22 dof, belongs here, because it is extended; however, the fit performed with the thermal model MEKAL in XSPEC, usually applied to galaxy clusters, is hardly acceptable, and it becomes so only after the addition of the simple model adopted for the unresolved sources: the parameters reported are those of the AGN immersed in the extended source.

The third subset (S3) comprises sources without a spectroscopic redshift. In terms of number of dof they are a mix of spectra of the type in S1 and S2. Following the same fit and error procedures, to show the redshift effect on the results, the spectra were attributed two fiducial values of z , equal to 1 and 2. The results for the 11 S3 sources are presented in Table 3, with the same structure as the previous tables separately for the two values of z , except that the flux is reported once for each source under $z=2$, because it is very similar to that obtained with $z=1$; in the second last column the R magnitude of the optical counterpart is reported. Given this magnitude, four of them could have been spectroscopically identified: rather than assigning to them an average value of z using those identified and with similar magnitude, since they are already well represented by the latter, it was decided to leave them out from the sample analysis in the next sections, hence no attempt was made to assign them a luminosity. Conversely, for the sources fainter than $R=23$, in the last column an X-ray luminosity is given, that has been evaluated, following Paper IV, as will be explained in Sect. 4.2.

The remaining spectra were treated with the C statistic, and the results are separately presented in Table 4 for the subset S4 (13 sources with known z , same structure as Table 2), and in Table 5 for the subset S5 (13 sources with unknown z , same structure as Table 3). In S4 there is one source for which N_H is unconstrained (likely due to spectral complexity combined with poor count statistics); it will therefore be excluded from the statistical considerations. In S5 five sources have their optical counterparts brighter than $R=23$, and will be treated like the similar sources in S3, as explained above.

Note that, despite the lower number of counts, in S4 and S5 the 2-10 keV fluxes observed, as estimated from the images and reported in Paper IV, are in the same range of values as in S2 and S3. This can be due either to larger off-axis angles or to a higher incidence of large N_H values. The distribution of the off-axis angles in the S2+S3 sample is however fully consistent with that in the S4+S5 sample (probability of 50% using the Kolmogorov-Smirnov test). On the other hand the distributions of the best fit $\log N_H$ differ with a probability higher than 99.98% and the median best fit $\log N_H$ with their interquartile ranges are 21.5 ± 1.8 and 23.2 ± 0.6 for the S2+S3 and S4+S5 samples respectively. As an example, Fig. 2 shows the spectral counts of two sources in the field of PKS0312-77 at similar off-axis angles: it is clear that the difference in the total number of counts is due to a substantial difference in N_H .

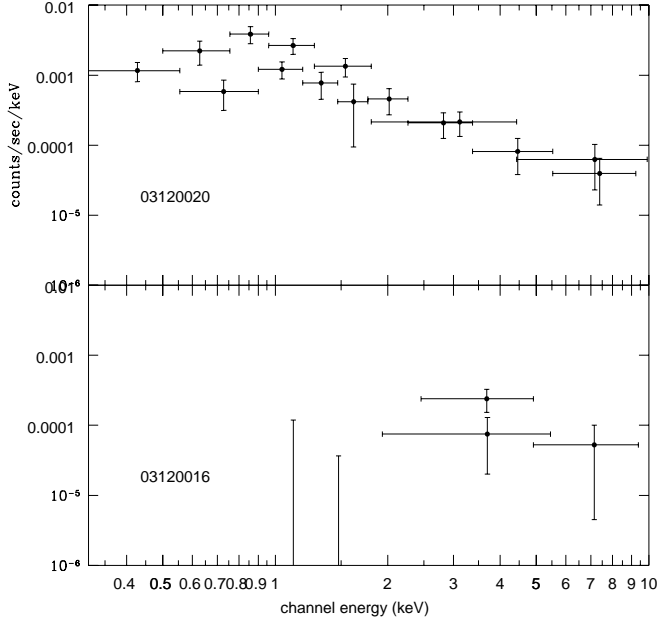


Fig. 2. The X-ray spectral count distributions of two sources with comparable 2–10 keV fluxes. At the top the unabsorbed source 03120020, at the bottom the source 03120016, which is evidently affected by strong absorption.

In Appendix 1 and 2, a comparison is drawn between the values of the flux (estimated directly from the images) and of N_H (estimated from a count hardness ratio) adopted in Paper IV, and the same values obtained from the spectral fits.

4. A synthesis of the results

4.1. The N_H distribution as a function of the flux

After the exclusions motivated in the previous section, the sample is now reduced to 107 sources. From their spectral fits, they can be subdivided into three categories, according to the best fit value of N_H : those with $N_H < 10^{22}$ cm $^{-2}$, those with N_H between 10^{22} and 10^{23} cm $^{-2}$, those with $N_H > 10^{23}$ cm $^{-2}$. For the sources without redshift there is of course a difference according to whether $z=1$ or 2 is adopted: in this case the source numbers in each category were first obtained separately with $z=1$ and with $z=2$, then their mean value was used. Fig. 3 shows a histogram of the F_u distribution of the 107 sources, where those falling into each of the three categories are indicated.

From Fig. 3 it can be immediately appreciated that, with the exception of the brightest one, 106 sources have fluxes between 0.8×10^{-14} and 20×10^{-14} erg cm $^{-2}$ s $^{-1}$. This sample can be subdivided into two flux intervals, defined as follows. In F_{u1} (from 0.8×10^{-14} to 5×10^{-14} erg cm $^{-2}$ s $^{-1}$) there are 82 sources, with a median flux equal to 2.4×10^{-14} erg cm $^{-2}$ s $^{-1}$; in F_{u2} (from 5×10^{-14}

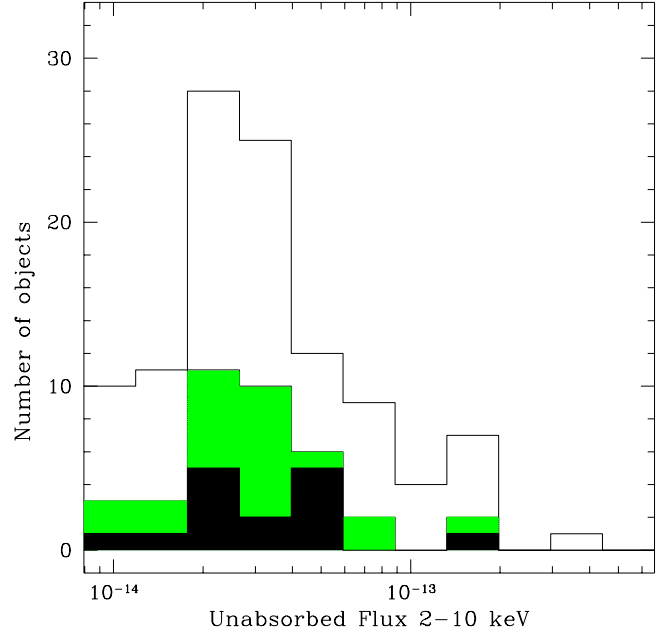


Fig. 3. The distribution as a function of F_u of the sources in the sample. See text for the sources excluded from this plot. In black the sources with $N_H > 10^{23}$ cm $^{-2}$, in gray those with N_H between 10^{22} and 10^{23} cm $^{-2}$, in white those with $N_H < 10^{22}$ cm $^{-2}$.

to 20×10^{-14} erg cm $^{-2}$ s $^{-1}$) there are 24 sources, with a median flux equal to 10×10^{-14} erg cm $^{-2}$ s $^{-1}$.

The fraction of sources for each of the three categories defined above, separately for the two flux intervals, is given in Table 6.

Table 6. Fraction of absorbed sources^c

N_H (cm $^{-2}$)	$< 10^{22}$	$10^{22} - 10^{23}$	$> 10^{23}$
F_{u1} ^a	52.5/82	19/82	12.5/82
	48.5/82	20.8/82	12.7/82
F_{u2} ^b	18/24	3/24	1/24
	17.9/24	3.1/24	3.0/24

^a F_{u1} : interval from 0.8×10^{-14} to 5×10^{-14} erg cm $^{-2}$ s $^{-1}$; ^b F_{u2} : interval from 5×10^{-14} to 20×10^{-14} erg cm $^{-2}$ s $^{-1}$; ^c The fractions in the two lines for each flux interval were obtained as described in the text (Sect. 4.1).

In order to take into account the uncertainties associated to the best fit values of the absorption columns, a procedure was set up to weigh each source with the prob-

ability that it falls into each of the N_H categories. This procedure is based on an analytic approximation (which turns out to resemble closely the combination of two gaussians with different sigmas, one for the values above, the other for those below the best fit N_H) to the probability distribution of N_H , estimated with XSPEC, using the STEPPAR command, for a number of objects selected in such a way as to properly represent the sources in the five subsets. The results differ only slightly from the previous ones, and are also given in Table 6, the second line for each of the two flux intervals. In the following the results obtained in this way will be used.

4.2. Fraction of absorbed sources as a function of the luminosity

The spectral fit results can also be used to diagnose whether the strength of the photoelectric absorption might be a function of the luminosity. Despite the relatively minor numerical contribution of the S3 and S5 sources with R fainter than 23, a higher fraction of them, compared with the other subsets, is affected by large values of N_H , and cannot therefore be dismissed. To avoid a fictitious concentration of them around some value of the luminosity if a nominal fixed value of z were adopted, a stochastic procedure, based on the ratio between X-ray and optical fluxes (X/O), already adopted in Paper IV, was followed to assign individual values of z . These values are given in Table 7, and the luminosities in Tables 3 and 5 were calculated accordingly. We note that the estimated values of z are roughly in agreement with the limits photometrically derived, for some of them, using the $R-K$ colour by Mignoli et al. (2004). In addition, we point out that Table 6 would not be significantly different if these values of z had been used in the spectral fitting.

Table 7. Estimated values of z for 15 sources with $R > 23$

source ID	z_{est}
03120031	1.3
03120036	2.0
03120045	1.7
03120065	1.0
26900029	2.3
26900075	1.9
05370022	1.0
05370054	2.1
05370060	1.4
05370072	1.4
05370091	0.8
05370111	1.7
05370153	1.8
05370157	1.6
0537052b	1.3

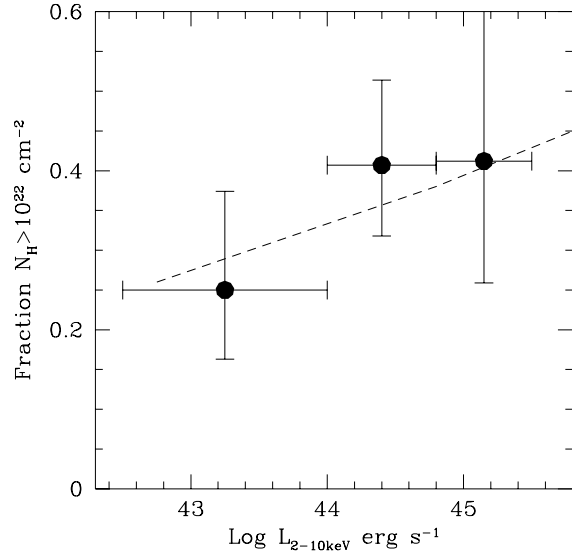


Fig. 4. The fraction of sources with $N_H > 10^{22} \text{ cm}^{-2}$ (68% poissonian errors) as a function of their luminosity. The sources with unknown z are included, as explained in the text. The broken line represents the expectation if such a fraction is intrinsically independent of the luminosity, but see text for comments on this issue in Sect. 4.2 and Sect. 5.

The result given in Fig. 4 shows no evidence of a luminosity dependence. However, to judge this result properly, it is necessary to take into account the selection effects introduced by the inhomogeneity of the flux limit within any XMM image. The broken line in the same figure, in very good agreement with the data points, takes this bias into account, on the basis of assumptions to be described in Sect. 5, among which there is one, immediately relevant to the issue, which states that the fractional distribution of N_H is independent of the luminosity. It must be stressed, however, that the latter statement is of restricted value, and need not remain valid when deeper X-ray surveys are also taken into consideration (see Ueda et al. 2003). Such surveys are indeed necessary to expand our knowledge at higher redshifts and lower luminosities, in order to better investigate the incidence of absorption, its higher values in particular, than could be done within the flux limit of our sample, as already noted when comparing the subsets S4/S5 to the subsets S2/S3. This point will be revisited in Sect. 5.

4.3. N_H versus the ratio X/O and the optical spectroscopic classification

In Paper IV the existence was emphasized of a close correlation between the X/O ratio and the X-ray luminosity for objects optically classified as non-broad-line AGN.

Figure 5 illustrates the fact that the fraction of highly absorbed sources is greater for the large than for the small values of X/O , thus confirming the latter as a fairly reliable diagnostic parameter for a preliminary classification of high luminosity, high obscuration AGN. Indeed, 16 out of the 57 objects with $\log L_{2-10\text{keV}} > 44$ in the sample of sources with spectroscopic redshifts (S1+S2+S4) have best fit $\log N_H > 22$ (11 of these objects have $\log N_H > 22$ at $> 90\%$ confidence level, 7 have best fit $\log N_H > 23$). If we consider also the sources without a spectroscopic redshift (S3+S5) to which a luminosity was assigned as described in Sect. 4.2, the number of high luminosity sources with $\log N_H > 22$ increases to 29 out of 71. The fraction of high luminosity AGN (QSO) obscured in X-rays is then at least 28%, most likely about 40%. This fraction can be translated, taking into account the sky coverage, into a surface density of highly obscured QSOs of $\sim 48 \text{ deg}^{-2}$, at the flux limit of $\sim 10^{-14} \text{ erg cm}^{-2} \text{ s}^{-1}$ of the HELLAS2XMM 1df survey. This density should be compared with the estimate (Mainieri et al. 2002) of $\sim 69 \text{ deg}^{-2}$, based on six objects only, in the 0.5–7 keV band at a flux limit of $1.6 \times 10^{-15} \text{ erg cm}^{-2} \text{ s}^{-1}$.

There are cases where the optical spectroscopic classification turns out the opposite of the X-ray classification, when the latter is based on the X-ray obscuration (see in particular Akiyama et al. 2003, Brusa et al. 2003). In the S1, S2 and S4 subsets one finds five objects (six if 03120127, with its very large upper limit on N_H , is included) optically classified as AGN1, whose best fit $\log N_H$ is greater than 22. In one case, 05370175, the absorbing column is greater than 10^{23} at $> 90\%$ confidence level. The fraction, 5 or 6 out of 60, is about 10%, in agreement with the finding (3/29) by Page et al. (2003). We note that the 6 objects with $\log N_H > 22$ all have $\log L_{2-10\text{keV}} > 44$, while the 17 AGN1 with $\log L_{2-10\text{keV}} < 44$, i.e. the Seyfert 1 objects, have $\log N_H < 22$: this difference cannot be attributed to a redshift dependent bias, however its significance is not high, according to the Fisher exact probability test (Siegel 1956) it amounts only to 89%.

The anomalous cases might reflect the existence of substantial variance in the dust to gas ratio, or alternatively of a geometrical separation with respect to the line of sight between the X-ray absorbing gas and the gas and dust in front of the broad line region. From a purely empirical side, one should not forget that variability may also play a role. One example is NGC 4151, which is characterized by a fairly dense, and variable, X-ray absorbing column; this object, when it was repeatedly observed with the IUE satellite, in some epochs simultaneously in the X-rays with EXOSAT, displayed impressive differences in the width of the permitted lines, from very broad to very narrow, correlated with changes in brightness, but without any evident correlation with the amount of N_H (Perola et al. 1986, Fiore et al. 1990, Ulrich 2000 and references therein). None of these hypotheses, though, give an obvious answer to the question why the anomalous cases should appear to be more common at QSO luminosities.

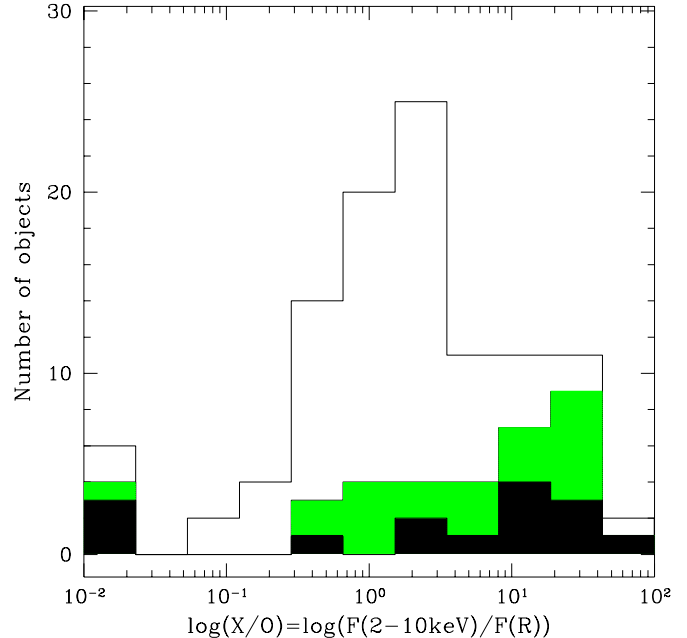


Fig. 5. The X/O distribution for the sources in the sample. In black the sources with $N_H > 10^{23} \text{ cm}^{-2}$, in gray those with N_H between 10^{22} and 10^{23} cm^{-2} , in white those with $N_H < 10^{22} \text{ cm}^{-2}$.

One also finds four objects classified as AGN2, with $\log N_H$ less than 22. Here the most probable origin of the discrepancy is the complexity of the X-ray spectra, which is found in detailed studies of bright sources (e. g. Turner et al. 2000, for the variable case of NGC 7582). As noted in Sect. 3, the simple model fit adopted aims to obtain an effective value of N_H , which for this paper is the relevant quantity.

5. Discussion

In Fig. 6 the fractions of objects with $\log N_H$ greater than 22, from Table 6, second line for each of the two flux intervals, are reproduced. The error bars (68%) are based purely on poissonian statistics, for an immediate comparison with the results collected in Piconcelli et al. (2003).

In the same figure the solid line represents the prediction of one of the so far most popular XRB synthesis models (Comastri et al. 1995, see also Comastri et al. 2001 for the N_H distribution), the dashed line model B in Gilli et al. (2001). The binomial distribution is used to estimate the significance of the discrepancy between the two

predictions and the observational results. This significance turns out equal to 99.999% for both models.

This result consolidates the finding by Piconcelli et al. (2003), based on an XMM–Newton sample, comparable in size and flux coverage with the one used here (15 sources are in common with the present sample) but with a much lower percentage of spectroscopic identifications (about 40%). It also supports the findings by Mainieri et al. (2002, as derived from their sample analysis by Piconcelli et al. 2003) with XMM–Newton in a flux interval similar to that considered in this paper, by Akiyama et al. (2000) with ASCA around 5×10^{-13} erg cm $^{-2}$ s $^{-1}$, and by Caccianiga et al. (2004) with XMM–Newton around 10^{-13} erg cm $^{-2}$ s $^{-1}$.

For flux values between 1 and 8×10^{-15} erg cm $^{-2}$ s $^{-1}$ Fig. 6 shows our estimates (again with 68% poissonian errors) derived from data on the Chandra Deep Field North (CDFN) given in Brandt et al. (2001) and Barger et al. (2002). The values of N_H were obtained from flux hardness ratios, thus they are not as reliable as those obtained from a spectral fit. Taking these estimates at face value, the discrepancy seems to disappear as one goes below $F_u = 10^{-14}$ erg cm $^{-2}$ s $^{-1}$.

To investigate the origin of the discrepancy, given the modest difference in the predictions of the two models, one can concentrate for simplicity on the first. To this effect it is useful to recall the three main assumptions in Comastri et al. (1995), namely: a) the LF is characterized by a double power law shape and pure luminosity evolution (PLE); b) the fractional distribution of the N_H values is independent of source luminosity and redshift; c) this distribution is *adjusted* to comply with the spectral shape of the XRB.

The broken line in Fig. 7 represents the expectation for the sample of objects used here, when the assumptions a) and b) are maintained, but, as an exercise, the N_H distribution is adopted, which corresponds to the broken line in Fig. 4. This distribution differs substantially from the one given in Comastri et al. (2001). The fractional value, per $\log N_H$ decade, is 0.3 between 20 and 21, then it drops to 0.175 and stays constant up to $\log N_H = 25$, a column density above which the absorber is Compton thick, to the extent that the direct emission is practically undetectable between 2 and 10 keV in the flux range explored. Correspondingly, Fig. 7 shows a prediction which is radically different from the one in Fig. 6, and, not surprisingly after the agreement found in Fig. 4, is in reasonably good agreement with the results from this sample. Notably though, the CDFN points are now in excess with respect to the prediction.

The conclusion from this exercise is that, down to a flux level where only 35% of the XRB is resolved, in order to better reproduce the observations a change in the N_H distribution would be sufficient. It goes almost without saying that the same exercise (the N_H distribution being different from the one adopted in Comastri et al. 1995, 2001) fails to reproduce satisfactorily the spectral shape of the XRB. Thus a more complex approach is needed,

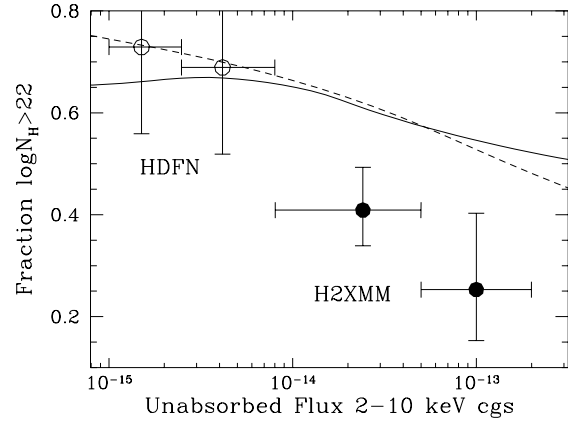


Fig. 6. The fraction of sources with $\log N_H$ greater than 22, in the two F_u intervals from Table 6 (full circles), compared with the predictions based on the model (solid line) by Comastri et al. (1995, see also Comastri et al. 2001), and the model B (dashed line) by Gilli et al. (2001). The points in the two lower flux intervals (empty circles) were derived from the CDFN survey (see text).

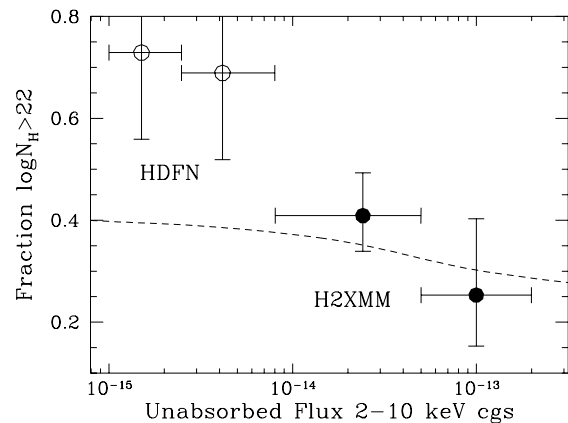


Fig. 7. The fraction of sources as in Fig. 6, here compared with the prediction which is obtained when, in the Comastri et al. (1995, 2001) model, the N_H distribution is changed to a flat one, as described in the text.

like the one followed by Ueda et al. (2003), which takes into account simultaneously the LF, its evolution, and the N_H distribution, the latter in principle as a function of luminosity and redshift: but this approach can only be pursued using a sample encompassing wider flux and luminosity ranges, as anticipated in Sect. 4.2, and is being pursued using the full sample adopted in Paper IV (La Franca et al., in prep.).

6. Conclusions

Starting from 117 sources from the HELLAS2XMM 1df survey (Paper IV), after the exclusion of 1 source with N_H unconstrained and 9 sources with unknown z and $R < 23$, the spectroscopic analysis of the remaining 107 X-ray spectra (86% with spectroscopic redshift) led to the following main result. The fraction of the 106 sources with $\log N_H > 22$ in the flux interval $0.8\text{--}20 \times 10^{-14}$ erg cm $^{-2}$ s $^{-1}$ is inconsistent, at the 99.999% confidence level, with the predictions of two well known XRB synthesis models, one by Comastri et al. (1995), the other by Gilli et al. (2001, their model B). This result consolidates the discrepancy also found by other authors in this flux interval, as mentioned in the previous section.

As an exercise for the Comastri et al. (1995) model, leaving unchanged all other assumptions, the adoption of a simple and different intrinsic distribution of the source percentage per decade of N_H , from $\log N_H = 20$ to 25 (which is consistent with the results from the present sample, see Fig. 4), leads to a much better agreement down to 10^{-14} erg cm $^{-2}$ s $^{-1}$, but fails to reproduce the much larger percentage of absorbed sources, derived from the CDFN survey, in the 10^{-15} to 10^{-14} erg cm $^{-2}$ s $^{-1}$ flux interval.

A study encompassing a much wider flux range, with a sufficiently large sample of objects (such as the one used in Paper IV), that should tackle simultaneously the problems of the shape and evolution of the LF, of the N_H distribution as a function of luminosity and cosmic epoch and eventually the XRB synthesis (with an approach akin to that followed by Ueda et al. 2003), goes beyond the scope of the present paper, and will be the subject of La Franca et al. (in prep.).

An important result, which basically confirms what was found in Paper IV, is that in our sample at least 28%, most likely about 40% of AGN with $\log L_{2-10\text{keV}} > 44$ (that is of the QSO) are obscured in X-rays ($\log N_H > 22$). This fraction can be translated, taking into account the sky coverage, into a surface density of highly obscured QSO of ~ 48 deg $^{-2}$, at the flux limit of $\sim 10^{-14}$ erg cm $^{-2}$ s $^{-1}$ of the HELLAS2XMM 1df survey.

As a side issue, note that in the sample studied, while a value of the parameter $\log(X/O)$ much greater than unity confirms itself to be strongly indicative of high obscuration in high luminosity AGN, as shown in Paper IV, there are 5 or 6 out of 60, that is about 10% of sources, with $\log N_H > 22$, that are optically classified as AGN1, in agreement with a previous finding by Page et al. (2003; see also Brusa et al. 2003, Akiyama et al. 2003). Notably they are all concentrated at $\log L_{2-10\text{keV}} > 44$. Among various possibilities, it is pointed out that variability may be one of the causes of this inconsistency.

7. Appendix 1

In Paper IV the source fluxes were derived directly from the counts image, with a conversion factor appropriate to

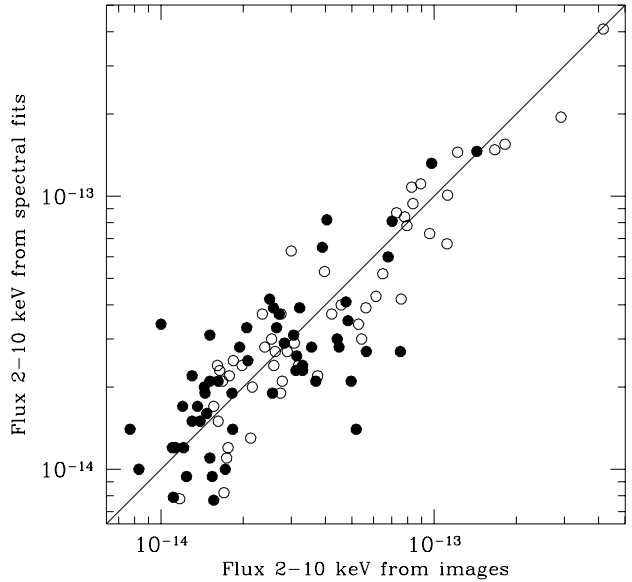


Fig. 8. Comparison of the best fit flux with that obtained from the images and used in Paper IV. Open circles are objects with $N_H < 10^{22}$ cm $^{-2}$, filled circles are objects with $N_H > 10^{22}$ cm $^{-2}$. The solid line represents a one to one relationship.

the filter in front of the camera and to a spectral shape with $\Gamma = 1.8$. In Fig. 8 these fluxes are compared with those obtained from the detailed spectral fits presented here, which are more accurate. The correlation is evidently good, and the points are distributed uniformly around a one to one relationship; no large systematic deviation in one sense or the other occurs when computing fluxes from the images, using the recipe of Baldi et al. (2002). This applies to both unobscured and obscured sources. On the other hand, there is a scatter which obviously increases toward low fluxes. The standard deviation of the ratio between the two flux estimates is 50% and 30% in the F_1 and F_2 flux ranges respectively.

8. Appendix 2

In Paper IV the values of N_H individually used to correct the observed flux, and hence the luminosity, for absorption were obtained by means of a count Softness Ratio (SR). These values are given in Fig. 9 against those obtained from the spectral fits (for the sources with a spectroscopic redshift). As for the flux values in Fig. 8, a rather satisfactory correlation is present with the values obtained from the spectral fits. The obvious limitation in the SR technique is that the error estimate is less reliable, but in a statistical sense the results obtained with this simple approach are sufficiently representative of the sample properties. Nevertheless, Fig. 9 suggests the presence of a systematic error affecting one of the two N_H estimates

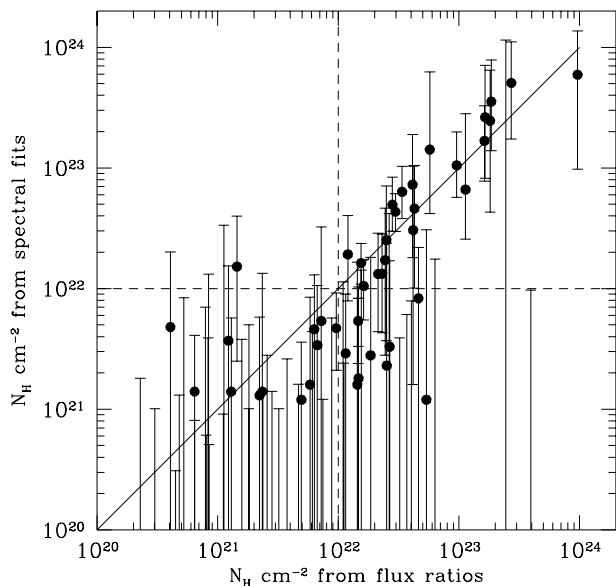


Fig. 9. Comparison of the best fit values of N_H (with 90% error bars) to those estimated with the Softness Ratio technique used in Paper IV. The solid line represents a one to one relationship, the two dashed lines divide the figure in four quadrants with $\log N_H$ higher or lower than 22.

(very likely that obtained from the SR). The number of objects in the lower-right quadrant is significantly higher than that in the upper-left quadrant, that is the SR technique provided a slightly higher number of objects with a “nominal” $22 < \log N_H < 22.5$. A nice correlation is recovered for higher values of the absorbing column, which are of course easier to detect. From this experience one might conclude, as a cautionary remark, that the SR technique tends to over-estimate the true value of the absorbing column around $\log N_H = 22$ by ≈ 0.3 .

9. Acknowledgments

Financial support is acknowledged from the italian MIUR (Cofin-03-2-23), INAF (grant 270/3003) and ASI (grant I/R/057/02).

References

Akiyama, M., Ohta, K., Yamada, T., et al. 2000, *ApJ*, 532, 700
 Akiyama, M., Ueda, Y., Ohta, K., Takahashi, T., Yamada, T. 2003, *ApJS*, 148, 275
 Alexander, D. M., Bauer, F.E., Brandt, W.N., et al. 2003a, *AJ*, 125, 383
 Alexander, D. M., Bauer, F.E., Brandt, W.N., et al. 2003b, *AJ*, 126, 539
 Baldi, A., Molendi, S., Comastri, A., et al. 2002, *ApJ*, 564, 190
 Barger A., Cowie L., Brandt, W.N., et al. 2002 *AJ*, 124, 1839
 Brandt, W.N., Alexander, D.M., Hornschemeier, A.E., et al. 2001 *AJ*, 122, 2810

Brusa, M., Comastri, A., Mignoli, M., et al. 2003, *A&A*, 409, 65
 Caccianiga, A., Severgnini, P., Braito, V., et al. 2004, *A&A*, in press, astro-ph/0312344
 Cash, W. 1979, *ApJ*, 228, 939
 Comastri, A., Setti, G., Zamorani, G., Hasinger, G. 1995, *A&A*, 296, 1
 Comastri, A., Fiore, F., Vignali, C., et al. 2001, *MNRAS*, 327, 781
 Fiore, F., Perola, G.C., Romano, M. 1990, *MNRAS*, 243, 522
 Fiore, F., Brusa, M. Cocchia, F., et al. 2003, *A&A*, 409, 79, Paper IV
 Giacconi, R., Rosati, P., Tozzi, P., et al. 2001, *ApJ*, 551, 664
 Giacconi, R., Zirm, A., Wang, J.X., et al. 2002, *ApJS*, 139, 369
 Gilli, R., Salvati, M., Hasinger, G. 2001, *A&A*, 366, 407
 Hasinger, G., Burg, R., Giacconi, R., et al. 1998, *A&A*, 329, 482
 Hasinger, G., Altieri, B., Arnaud, M., et al. 2001, *A&A*, 365, L45
 Mainieri, V., Bergeron, J., Hasinger, G., et al. 2002, *A&A*, 393, 425
 Mignoli, M., Pozzetti, L., Comastri, A., et al. 2004, *A&A*, in press, astro-ph/0401298
 Miyaji, T., Hasinger, G., Schmidt, M. 2000, *A&A*, 353, 25
 Moretti, A., Campana, S., Lazzati, D., Tagliaferri, G. 2003, *ApJ*, 588, 696
 Mushotzky, R.F., Cowie, L.L., Barger, A.J., & Arnaud, K.A. 2000, *Nature*, 404, 459
 Page, M.J., McHardy, I.M., Gunn, K.F., et al. 2003, *AN*, 324, 101
 Perola, G.C., Piro, L., Altamore, A., et al. 1986, *ApJ*, 306, 508
 Piconcelli, E., Cappi, M., Bassani, L., Di Cocco, G., Dadina, M. 2003, *A&A*, 412, 689
 Setti, G. & Woltjer, L. 1989, *A&A*, 224, L21
 Siegel, S. 1956, *Non Parametric Statistics*, New York: McGraw-Hill
 Strüder, L., Briel, U., Dennerl, K., et al. 2001, *A&A*, 365, L18
 Turner, T.J., Perola, G.C., Fiore, F., et al. 2000, *ApJ*, 531, 245
 Turner, M.J.L., Abbey, A., Arnaud, M., et al. 2001, *A&A*, 365, L27
 Ueda, Y., Akiyama, M., Ohta, K., Miyaji, T. 2003, *ApJ*, 598, 886
 Ulrich, M.-H. 2000, *A&Ap Rev*, 10, 135
 Wilman, R.J. & Fabian, A.C. 1999, *MNRAS*, 309, 862

Table 1. Spectral fits of the subset S1

source ID	type	z	inst	N_H^a	Γ	χ^2/dof	F^b	F_u^b	$\log L_{2-10\text{keV}}^c$
03120002	AGN1	1.187	pm	<0.05	$1.88 \pm_{0.06}^{0.07}$	190.0/183	41.0	41.3	45.48
03120003	AGN1	0.420	pm	<0.03	$1.98 \pm_{0.11}^{0.12}$	88.4/72	14.8	14.9	43.97
03120004	AGN1	0.890	pm	<0.08	$2.44 \pm_{0.15}^{0.16}$	62.6/53	5.2	5.2	44.43
03120005	AGN1	1.274	pm	<0.14	$1.83 \pm_{0.15}^{0.16}$	43.3/46	9.4	9.4	44.89
03120006	AGN2	0.680	pm	<0.16	$1.56 \pm_{0.14}^{0.17}$	33.1/39	10.8	10.8	44.24
03120007	AGN1	0.381	m	$0.12 \pm_{0.12}^{0.24}$	$1.51 \pm_{0.35}^{0.41}$	17.0/18	19.5	19.7	43.93
03120009	AGN1	1.522	pm	<0.84	$1.86 \pm_{0.33}^{0.49}$	16.4/19	2.4	2.4	44.49
03120010	AGN1	0.246	pm	<0.14	$2.69 \pm_{0.48}^{0.79}$	24.1/19	1.3	1.3	42.44
03120012	AGN1	0.507	pm	<0.24	$2.49 \pm_{0.44}^{0.79}$	20.0/16	2.1	2.2	43.43
03120013	AGN1	1.446	pm	$0.71 \pm_{0.71}^{2.10}$	$2.83 \pm_{0.80}^{1.51}$	18.4/14	0.8	0.8	44.34
03120014	ELG	0.206	pm	<0.26	$1.54 \pm_{0.31}^{0.53}$	21.5/18	5.3	5.3	42.78
03120017	ETG	0.320	pm	$0.13 \pm_{0.13}^{0.45}$	$2.28 \pm_{0.66}^{1.15}$	14.1/11	1.9	2.0	42.86
03120018	ETG	0.159	pm	$0.46 \pm_{0.46}^{0.84}$	$1.87 \pm_{0.78}^{1.08}$	22.4/14	2.4	2.5	42.23
03120020	ELG	0.964	pm	<0.70	$2.03 \pm_{0.41}^{0.70}$	9.5/12	2.4	2.4	44.07
03120021	AGN1	2.736	pm	<4.19	$1.53 \pm_{0.52}^{0.69}$	10.4/11	2.1	2.2	44.87
03120028	ELG	0.641	pm	$0.54 \pm_{0.54}^{2.70}$	$1.63 \pm_{0.80}^{1.54}$	9.8/12	2.2	2.2	43.51
26900001	AGN1	0.336	pm	<0.06	$1.78 \pm_{0.14}^{0.20}$	42.8/43	8.4	8.4	43.47
26900002	AGN1	0.850	pm	$0.54 \pm_{0.30}^{0.29}$	$1.63 \pm_{0.24}^{0.28}$	32.4/30	14.6	14.8	44.62
26900003	AGN1	0.433	pm	<0.08	$2.13 \pm_{0.20}^{0.29}$	33.1/34	6.7	6.7	43.68
26900004	AGN1	0.284	pm	<0.05	$2.03 \pm_{0.21}^{0.26}$	30.4/26	7.8	7.8	43.3
26900007	AGN1	1.234	pm	<0.29	$2.07 \pm_{0.32}^{0.43}$	14.9/12	2.1	2.1	44.29
26900010	AGN1	1.355	pm	<0.38	$1.91 \pm_{0.37}^{0.47}$	8.5/10	2.9	2.9	44.47
26900012	AGN1	0.433	pm	$0.14 \pm_{0.14}^{0.27}$	$2.66 \pm_{0.69}^{1.09}$	7.4/15	0.8	0.8	42.85
26900015	AGN1	1.610	pm	$1.52 \pm_{1.27}^{2.47}$	$2.72 \pm_{0.74}^{1.28}$	8.8/14	1.1	1.1	44.57
05370002	AGN1	1.244	pm	<0.10	$1.95 \pm_{0.09}^{0.10}$	85.0/96	15.5	15.5	45.13
05370003	AGN1	0.317	pm	<0.10	$2.04 \pm_{0.19}^{0.23}$	37.1/52	10.1	10.1	43.53
05370004	AGN1	0.894	pm	<0.24	$1.58 \pm_{0.14}^{0.20}$	55.9/47	8.1	8.1	44.39
05370005	AGN1	1.158	pm	$0.16 \pm_{0.16}^{0.69}$	$1.60 \pm_{0.34}^{0.42}$	15.7/14	11.1	11.1	44.79
05370007	AGN1	0.842	pm	<0.14	$1.91 \pm_{0.25}^{0.34}$	20.9/21	2.7	2.7	43.94
05370008	AGN2*	0.379	pm	<0.18	$2.29 \pm_{0.33}^{0.48}$	17.8/25	3.9	4.0	43.34
05370009	AGN1	0.770	pm	$0.14 \pm_{0.14}^{1.20}$	$2.10 \pm_{0.53}^{1.28}$	16.8/16	2.2	2.2	43.81
05370013	AGN1	0.901	pm	<0.39	$1.85 \pm_{0.35}^{0.53}$	11.5/11	3.0	3.0	44.04
05370014	AGN1	1.659	pm	<1.32	$1.25 \pm_{0.35}^{0.54}$	7.7/14	6.3	6.3	44.74
05370015	AGN1	0.880	pm	$0.37 \pm_{0.37}^{1.17}$	$2.32 \pm_{0.78}^{1.53}$	11.6/13	2.4	2.5	44.07
05370016	AGN2	0.995	pm	$1.32 \pm_{0.88}^{1.56}$	$2.05 \pm_{0.52}^{0.81}$	9.8/17	3.5	3.6	44.28
05370017	AGN1	0.904	pm	<0.28	$1.86 \pm_{0.36}^{0.54}$	6.4/9	2.7	2.7	44.0
05370021	ELG*	1.192	pm	$0.16 \pm_{0.16}^{1.50}$	$1.54 \pm_{0.54}^{0.99}$	9.0/11	3.9	3.9	44.34
05370024	ETG	0.075	pm	<0.12	$1.18 \pm_{0.36}^{0.42}$	19.0/12	4.0	4.0	41.72
0537011a	AGN2	0.981	pm	$1.33 \pm_{0.90}^{1.50}$	$1.88 \pm_{0.40}^{0.63}$	26.7/16	4.1	4.2	44.29
50900020	AGN1	0.770	m	$0.48 \pm_{0.48}^{1.53}$	$2.42 \pm_{0.37}^{1.51}$	5.1/8	4.2	4.3	44.18
50900031	AGN1	0.556	m	<0.10	$1.83 \pm_{0.64}^{0.67}$	21.2/11	4.3	4.3	43.69
15800001	AGN1	1.211	m	<0.31	$2.12 \pm_{0.22}^{0.36}$	14.8/19	8.7	8.7	44.91
15800002	AGN1	0.848	m	<0.13	$1.94 \pm_{0.26}^{0.30}$	17.0/17	7.3	7.3	44.39
15800008	AGN1	1.151	m	<1.42	$1.43 \pm_{0.44}^{0.76}$	6.2/8	3.9	3.9	44.27

^a N_H in source frame, units of 10^{22} cm^{-2} ; ^b Flux in the 2–10 keV band, F: observed, F_u : corrected for absorption, in units of $10^{-14} \text{ erg cm}^{-2} \text{ s}^{-1}$; ^c Log of the luminosity in units of erg s^{-1} .

Table 2. Spectral fits of the subset S2

source ID	type	z	inst	N_H^a	Γ	χ^2/dof	F^b	F_u^b	$\log L_{2-10\text{keV}}^c$
03120008	ETG	0.052	pm	$0.15 \pm_{0.15}^{0.45}$	1.9	23.2/22	2.3	2.4	41.19
03120011	AGN1	0.753	pm	<0.24	1.9	6.3/8	1.7	1.7	43.62
03120022	AGN1	2.140	p	$4.61 \pm_{3.60}^{5.85}$	1.9	9.1/6	3.7	3.8	45.06
03120024	AGN1	1.838	m	<3.36	1.9	1.9/5	1.2	1.2	44.41
03120034	AGN2	0.265	pm	$4.33 \pm_{1.35}^{1.81}$	1.9	10.4/6	13.2	16.2	43.54
03120066	AGN1	1.449	pm	<1.76	1.9	9.3/6	1.1	1.1	44.12
0312089a	ELG	0.809	m	$3.05 \pm_{2.89}^{7.34}$	1.9	9.4/7	2.2	2.4	43.85
26900006	AGN1	0.964	m	<0.09	1.9	5.3/8	14.5	14.5	44.81
26900009	AGN1	0.995	pm	$0.14 \pm_{0.14}^{0.43}$	1.9	4.6/8	2.0	2.0	43.98
26900016	AGN1	1.314	m	$0.34 \pm_{0.34}^{0.72}$	1.9	2.3/6	3.7	3.7	44.54
26900022	AGN2	0.592	pm	$1.05 \pm_{0.50}^{0.69}$	1.9	4.3/6	2.6	2.7	43.57
26900028	AGN1	0.738	pm	<0.33	1.9	9.0/5	2.4	2.4	43.75
26000038	ELG	0.904	pm	$4.96 \pm_{1.96}^{3.42}$	1.9	1.9/5	3.5	3.9	43.9
26900039	AGN1	0.930	pm	$6.35 \pm_{2.54}^{3.95}$	1.9	6.3/6	6.5	7.2	44.47
05370019	AGN1	1.330	pm	<0.44	1.9	4.5/8	1.5	1.5	44.16
05370020	AGN1	0.763	m	<0.11	1.9	13.5/8	3.0	3.0	43.88
05370031	AGN1	3.276	pm	$0.12 \pm_{0.12}^{2.96}$	1.9	0.3/5	1.5	1.5	45.09
05370036	AGN1	1.329	m	<0.39	1.9	7.0/8	2.7	2.7	44.42
05370040	AGN1	1.485	pm	$0.28 \pm_{0.28}^{1.54}$	1.9	1.0/5	0.9	0.9	44.08
05370041	AGN1	1.644	pm	<0.79	1.9	11.5/7	0.8	0.8	44.1
05370043	AGN2	1.797	pm	$10.5 \pm_{4.8}^{9.4}$	1.9	4.6/8	3.1	3.4	44.83
05370123	AGN2*	1.153	m	$6.63 \pm_{4.06}^{21.58}$	1.9	7.2/5	2.7	3.0	44.32
05370135	AGN2	0.484	pm	$1.72 \pm_{1.44}^{2.93}$	1.9	0.6/5	1.2	1.3	43.05
0537042a	AGN1	1.945	pm	$0.33 \pm_{0.33}^{1.37}$	1.9	5.6/7	1.5	1.5	44.56
50900001	AGN2	1.049	m	<1.14	1.9	2.3/4	2.1	2.1	44.06
50900013	AGN2	1.261	m	$2.52 \pm_{2.15}^{4.58}$	1.9	6.8/6	3.0	3.1	44.42
50900036	AGN2	0.694	m	<0.97	1.9	7.2/6	2.3	2.3	43.67
50900039	AGN1	0.818	m	<0.83	1.9	6.2/5	1.4	1.4	43.62
50900061	ETG	0.324	m	$0.47 \pm_{0.26}^{0.45}$	1.9	10.8/7	3.7	3.8	43.11
50900067	AGN1	1.076	m	<0.57	1.9	5.8/7	3.4	3.4	44.3
15800005	AGN1	1.207	m	<0.13	1.9	8.7/8	3.7	3.7	44.45
15800011	AGN1	2.069	m	<0.50	1.9	1.5/4	2.5	2.5	44.85
15800012	AGN2	0.233	m	$1.63 \pm_{0.54}^{0.74}$	1.9	10.6/5	6.0	6.5	43.01
15800013	ELG	1.326	m	$1.92 \pm_{1.13}^{2.12}$	1.9	6.7/5	1.9	2.0	44.29
15800017	AGN1	1.946	m	<0.61	1.9	4.1/6	2.9	2.9	44.85
15800019	AGN2	1.957	m	$7.26 \pm_{5.45}^{11.67}$	1.9	6.7/5	2.3	2.5	44.79

^a N_H in source frame, units of 10^{22} cm^{-2} ; ^b Flux in the 2–10 keV band, F: observed, F_u : corrected for absorption, in units of $10^{-14} \text{ erg cm}^{-2} \text{ s}^{-1}$; ^c Log of the luminosity in units of erg s^{-1} .

Table 3. Spectral fits of the subset S3

source ID	inst	N_H^a	Γ	χ^2/dof	N_H^a	Γ	χ^2/dof	F^b	F_u^b	R^c	$\log L_{2-10\text{keV}}^d$
		$z = 1$			$z = 2$						
03120029	pm	<0.56	1.9	8.2/8	<1.51	1.9	8.2/8	1.2	1.2	18.8	
03120031	pm	$1.58 \pm_{0.93}^{1.59}$	1.9	0.9/6	$4.38 \pm_{2.60}^{4.76}$	1.9	0.9/5	1.7	1.8	23.6	44.29
03120045	pm	$3.20 \pm_{1.82}^{3.34}$	1.9	6.1/8	$9.29 \pm_{5.46}^{10.76}$	1.9	6.2/8	2.8	3.0	24.4	44.81
03120065	pm	$1.15 \pm_{1.15}^{0.28}$	1.9	6.6/9	$3.22 \pm_{3.22}^{7.10}$	1.9	6.6/9	1.6	1.7	≥ 24	43.98
26900014	pm	$0.25 \pm_{0.25}^{0.64}$	$2.24 \pm_{0.61}^{0.80}$	7.0/9	$0.69 \pm_{0.69}^{1.73}$	$2.24 \pm_{0.61}^{0.79}$	7.0/9	1.4	1.4	21.6	
26900075	pm	$10.2 \pm_{5.9}^{14.2}$	1.9	0.3/4	$32.9 \pm_{20.2}^{44.7}$	1.9	0.4/4	3.3	4.0	24.6	45.05
05370010	pm	<0.45	$1.82 \pm_{0.52}^{0.75}$	12.3/15	<1.26	$1.83 \pm_{0.30}^{0.52}$	12.2/15	2.7	2.7	22.4	
05370012	pm	$0.03 \pm_{0.03}^{0.42}$	$1.83 \pm_{0.31}^{0.52}$	15.9/14	<1.24	$1.83 \pm_{0.30}^{0.52}$	15.9/14	2.4	2.4	22.5	
05370022	pm	$0.18 \pm_{0.18}^{0.38}$	1.9	7.5/6	$0.51 \pm_{0.51}^{1.04}$	1.9	7.5/6	2.8	2.8	≥ 23.0	44.19
05370054	pm	$0.78 \pm_{0.78}^{5.69}$	$1.69 \pm_{0.80}^{1.92}$	4.6/8	$1.68 \pm_{1.68}^{14.60}$	$1.61 \pm_{0.71}^{1.73}$	4.7/8	2.1	2.1	25.0	44.88
05370111	pm	$7.04 \pm_{4.12}^{9.66}$	1.9	3.3/8	$20.1 \pm_{12.2}^{26.5}$	1.9	3.8/8	2.1	2.3	24.5	44.69

^a N_H in source frame, $z=1$ or $z=2$, units of 10^{22} cm^{-2} ; ^b Flux in the 2–10 keV band, F: observed, F_u : corrected for absorption, in units of $10^{-14} \text{ erg cm}^{-2} \text{ s}^{-1}$; ^c R magnitude of optical counterpart; ^d Log of the luminosity in units of erg s^{-1} , only for sources with R greater than 23, for the redshift values given in Table 7 (see Sect. 4.2).

Table 4. Spectral fits of the subset S4

source ID	type	z	inst	N_H^a	Γ	Cst/bins	F^b	F_u^b	$\log L_{2-10\text{keV}}^c$
03120016	AGN2*	0.841	pm	$35.5 \pm_{21.6}^{43.1}$	1.9	22.6/24	3.1	5.3	44.23
03120035	AGN1	1.272	m	$0.23 \pm_{0.23}^{2.15}$	1.9	19.3/20	1.4	1.4	44.09
03120127	AGN1	2.251	pm	<115	1.9	15.6/18	3.4	3.4	45.07
03120181	ELG	0.709	pm	$24.6 \pm_{20.3}^{40.2}$	1.9	14.0/14	1.2	2.0	43.63
03120501	ETG	0.205	m	uncons	1.9	16.5/20	1.3	1.3	42.18
26900072	ELG	1.389	p	$59.3 \pm_{49.5}^{77.7}$	1.9	14.9/15	8.2	13.4	45.16
05370035	AGN1	0.897	p	$0.18 \pm_{0.18}^{0.85}$	1.9	13.3/11	0.9	0.9	43.55
05370078	AGN1	1.622	m	$14.2 \pm_{10.0}^{48.4}$	1.9	24.5/23	2.0	2.3	44.56
05370175	AGN1	1.246	pm	$50.7 \pm_{33.3}^{60.3}$	1.9	21.9/22	2.5	4.1	44.53
0537052a	AGN1	1.665	pm	$0.83 \pm_{0.83}^{1.36}$	1.9	31.6/20	0.8	0.8	44.12
15800025	ELG	0.470	m	$0.29 \pm_{0.28}^{0.61}$	1.9	16.3/15	1.9	1.9	43.18
15800062	AGN2	1.568	m	$26.3 \pm_{18.1}^{44.7}$	1.9	25.2/18	2.8	3.4	44.69
15800092	ELG	0.993	m	$16.8 \pm_{9.0}^{16.0}$	1.9	28.6/20	3.3	4.2	44.3

^a N_H in source frame, units of 10^{22} cm^{-2} ; ^b Flux in the 2–10 keV band, F: observed, F_u : corrected for absorption, in units of $10^{-14} \text{ erg cm}^{-2} \text{ s}^{-1}$; ^c Log of the luminosity in units of erg s^{-1} .

Table 5. Spectral fits of the subset S5

source ID	inst	N_H^a	Γ	Cst/bins	N_H^a	Γ	Cst/bins	F^b	F_u^b	R^c	$\log L_{2-10\text{keV}}^d$
		$z = 1$			$z = 2$						
03120036	p	$1.15 \pm_{0.98}^{1.35}$	1.9	12.3/18	$3.22 \pm_{2.72}^{3.93}$	1.9	13.1/18	1.9	1.9	24.6	44.79
03120124	m	$5.26 \pm_{3.27}^{5.54}$	1.9	11.0/17	$15.8 \pm_{10.1}^{18.6}$	1.9	11.1/17	2.2	2.4	22.5	
26900029	pm	$0.75 \pm_{0.57}^{0.90}$	1.9	14.2/19	$2.03 \pm_{1.53}^{2.60}$	1.9	14.3/19	2.8	2.8	25.1	45.11
05370037	p	$1.37 \pm_{0.93}^{1.82}$	1.9	17.9/19	$4.09 \pm_{2.83}^{4.77}$	1.9	17.5/19	4.4	4.5	21.5	
05370060	pm	$0.90 \pm_{0.90}^{1.93}$	1.9	18.5/23	$2.41 \pm_{2.41}^{5.45}$	1.9	18.5/23	1.0	1.0	23.9	44.11
05370072	pm	$5.65 \pm_{3.38}^{6.01}$	1.9	15.6/25	$16.9 \pm_{10.4}^{19.1}$	1.9	15.6/25	1.0	1.1	≥ 24	44.16
05370091	m	$24.7 \pm_{19.4}^{54.9}$	1.9	24.6/22	$55.5 \pm_{40.3}^{98.4}$	1.9	25.0/22	4.2	5.7	23.7	44.26
0537011b	m	$34.0 \pm_{24.9}^{61.6}$	1.9	7.7/11	$66.4 \pm_{26.3}^{86.2}$	1.9	9.2/11	1.4	2.0	21.7	
05370153	pm	$10.3 \pm_{7.1}^{16.0}$	1.9	25.2/24	$34.2 \pm_{23.9}^{48.0}$	1.9	25.2/24	1.2	1.4	≥ 24.6	44.54
05370157	pm	$11.4 \pm_{5.3}^{9.0}$	1.9	27.3/26	$33.0 \pm_{15.9}^{24.9}$	1.9	28.5/26	1.4	1.8	≥ 24.5	44.52
05370162	pm	$5.26 \pm_{4.00}^{11.00}$	1.9	32.5/20	$15.4 \pm_{12.2}^{36.7}$	1.9	32.7/20	1.3	1.5	21.6	
0537042b	m	$8.32 \pm_{4.63}^{18.90}$	1.9	15.6/13	$22.8 \pm_{12.8}^{36.4}$	1.9	16.5/13	2.2	2.5	21.5	
0537052b	m	$7.13 \pm_{3.93}^{6.35}$	1.9	11.7/14	$22.8 \pm_{13.0}^{20.9}$	1.9	11.4/14	1.7	2.0	23.7	44.34

^a N_H in source frame, $z=1$ or $z=2$, units of 10^{22} cm^{-2} ; ^b Flux in the 2–10 keV band, F: observed, F_u : corrected for absorption, in units of $10^{-14} \text{ erg cm}^{-2} \text{ s}^{-1}$; ^c R magnitude of optical counterpart; ^d Log of the luminosity in units of erg s^{-1} , only for sources with R greater than 23, for the redshift values given in Table 7 (see Sect. 4.2).